

Laser cluster interaction in external magnetic field: emergence of nearly mono-energetic weakly relativistic electron beam

Kalyani Swain,^{1,2} S. S. Mahalik,^{1,*} M. Kundu^{1,2}

¹*Institute for Plasma Research, Bhat, Gandhinagar, 382428, India*

²*Homi Bhabha National Institute, Training School Complex, Anushaktinagar, Mumbai 400094, India*

(Dated: March 6, 2023)

Recent studies [Sci Rep 12, 11256 (2022)] on laser interaction (wavelength 800 nm, intensity $> 10^{16}$ W/cm²) with deuterium nano-cluster in an ambient magnetic field (B_0) demonstrate that collisionless absorption of laser occurs in two stages via anharmonic resonance (AHR) and electron-cyclotron resonance (ECR) or relativistic ECR (RECR) processes. Auxiliary B_0 enhances coupling of laser to cluster-electrons via improved frequency-matching for ECR/RECR as well as phase-matching for prolonged duration of the 5-fs (fwhm) broadband pulse and the average absorbed energy per electron $\bar{\mathcal{E}}_A$ significantly jumps up $\approx 36 - 70$ times of its ponderomotive energy (U_p). In this paper, we report energy dispersion of these energetic electrons and their angular distribution in position and momentum space by performing hybrid-PIC simulations. By simulating bigger clusters (radius $R_0 \approx 3 - 4$ nm) at high intensities $\approx 10^{16} - 10^{18}$ W/cm², we find $\bar{\mathcal{E}}_A \approx 36 - 70 U_p$ similar to a small cluster ($R_0 \approx 2$ nm), but total energy absorption increases almost linearly with increasing cluster size due to more number of available energy carriers. And, in all cases (near ECR/RECR) electrons are collimated like a weakly relativistic gyrating beam (about B_0) within an angular spread $\Delta\theta < 5^\circ$, propagating far beyond $200R_0$ along B_0 . This study may be relevant because an intense, collimated electron beam has wide applications including the fast ignition technique for inertial confinement fusion, ultra-short x-ray sources and medical applications.

I. INTRODUCTION

The interaction of intense laser field with cluster of atoms or molecules (called nano-clusters) constitutes a promising research area in strong-field wave-matter interaction. Atomic-clusters, with locally high atom-density resembling those in a solid, may absorb 80 – 90% of laser compared to laser-solid and laser-atomic gas interactions[1]. Importantly, laser-cluster interaction (LCI) produces energetic ions[1–4], neutrals[5], electrons[2, 6–9] and x-rays[10–14], and thus paves the way to future generation particle accelerators and photon accelerators. Basic processes in LCI: (i) inner ionization —birth of electrons leading to formation of nano-plasma, (ii) outer ionization —removal electrons from the whole cluster, (iii) coulomb explosion —acceleration of background ions are described elsewhere[15–18], and not repeated here for the sake of conciseness.

For laser intensities $I_0 > 10^{16}$ W/cm² and wavelength $\lambda > 600$ nm, laser absorption in cluster is mostly collisionless[19–22] wherein linear resonance (LR) and anharmonic resonance (AHR) may play active roles. LR happens[23–26] for a long duration laser pulse (typically > 50 fs) on coulomb explosion of an initially over-dense ($\rho_i > \rho_c$) cluster when ionic charge density $\rho_i(t)$ gradually drops to the critical density $\rho_c = \omega^2/4\pi$ and the Mie-plasma frequency $\omega_M(t) = \sqrt{4\pi\rho_i/3}$ dynamically meets the laser frequency $\omega = 2\pi c/\lambda$. Atomic units (a.u.) $|e| = m_0 = \hbar = 4\pi\epsilon_0 = 1$ are used unless noted explicitly. However, for short pulse duration $\omega_M(t) > \omega$ holds (cluster is over-dense) and AHR becomes important. During AHR, oscillation frequency of an electron in the self-consistent anharmonic cluster-potential meets ω . AHR is noted in many works[27–33] using rigid sphere model

(RSM), particle-in-cell (PIC) and molecular dynamics (MD) simulations.

Though numerous experiments, analytical models and numerical simulations have shown energetic electrons in the collisionless regime, our survey[34] reveals that maximum average energy of a liberated electron mostly remains close to $\approx 3.17U_p$ similar to the laser-atom[35–37] interaction ($U_p = I_0/4\omega^2$ is the ponderomotive energy of an electron) or below; *even if* laser has adequate supply of energy. In case of laser-deuterium cluster interaction[34], with a 5-fs broadband laser pulse (central $\lambda = 800$ nm, $I_0 \approx 10^{16} - 10^{18}$ W/cm²) and an ambient magnetic field (B_0) in crossed orientation to the laser electric field (E_l), earlier we have shown by RSM and three dimensional PIC simulation that enhanced laser absorption occurs in two stages via AHR (1st stage) and electron cyclotron resonance (ECR) or relativistic ECR (RECR) processes (2nd stage). During ECR/RECR, electron cyclotron frequency $\Omega_c = |e|B_0/m_0\gamma = \Omega_{c0}/\gamma$ meets ω . The auxiliary B_0 enhances coupling of laser to cluster-electrons via improved frequency-matching as well as phase-matching and the average absorbed energy per electron jumps to $\bar{\mathcal{E}}_A \approx 36 - 70 U_p$ (more than 12 – 36 fold[34]) which is *significant*.

One may argue that required ambient $B_0 = 10 - 20$ kT is too high to achieve above ECR/RECR in a laboratory with 800 nm laser. With CO₂ laser ($\lambda \approx 10.6\mu\text{m}$), however, the strength of B_0 for the ECR/RECR is scaled down to $B_0 \approx 1 - 2$ kT which seems to be feasible (and our simulations are underway). Recent demonstration of pulsed magnetic fields from sub kilo-Tesla [38, 39] and kilo-Tesla to mega-Tesla [40–44] has renewed interest in laser-plasma [45–47] community and may serve the purpose. In this context, we mention that self-generated (quasi-static) magnetic fields beyond 10 kT are noted in high density laser-plasma experiments and astro-physical conditions. For example, self-generated magnetic fields $\approx 20 - 46$ kT have been measured [48, 49]. Magnetic fields around neutron stars and pulsars[50] typically vary

* Presently at Bellatrix Aerospace Pvt. Ltd., Bangalore, 560020, India

$\approx 10^1 - 10^5$ kT. Understanding of the origin of energetic electrons in these strong electromagnetic field conditions are also of fundamental interest. From the application point of view, energetic electrons produced by LCI via ECR/RECR in an ambient magnetic field can be helpful for the table-top radiation sources (such as x-rays), particle-accelerators useful for medical applications and inertial confinement fusion (ICF).

In the previous work[34], though it is shown that average energy of laser-driven cluster-electrons increases significantly ($\bar{\mathcal{E}}_A \approx 36 - 70U_p$) with an ambient B_0 near ECR/RECR, it is not yet known how those electrons propagate. Generation of relativistic electron beam (REB) is also of current interest[51–53]. Therefore, understanding the energy distribution of ejected cluster-electrons and their divergence (directional) properties are important from the point of view of applications as well as in the astrophysical scenario mentioned above. In this paper, we report energy dispersion of these energetic electrons and their angular distribution in position and momentum space by performing hybrid-PIC simulations. The effect of ambient magnetic field-driven ECR/RECR on different cluster size is also not known so far. This may be particularly important for higher electron flux as a collimated beam. By simulating relatively bigger clusters of radius $R_0 \approx 3 - 4$ nm at intensities $I_0 \approx 10^{16} - 10^{18}$ W/cm², here we find that average absorbed energy per electron jumps to $\bar{\mathcal{E}}_A \approx 36 - 70U_p$ similar to a small cluster ($R_0 \approx 2$ nm), but total energy absorption increases almost linearly with increasing cluster size due to more number of available energy carriers. And, in all cases (near ECR/RECR) electrons are collimated like a weakly relativistic gyrating beam (about B_0) within an angular spread $\Delta\theta < 5^\circ$, propagating far beyond $200R_0$ along B_0 .

In Sec.II laser pulse and cluster parameters are given. In Sec.III we discuss details of the PIC simulation code and its new hybrid capability for treating particle-interactions outside the simulation box. Section IV focuses on the energy distribution of electrons and their angular distribution in the position space (as well as in the momentum space) corresponding to the laser energy absorption by electrons for different ambient B_0 . In Sec.V, laser energy absorption for bigger clusters and associated angular distributions of ejected electrons are compared at high intensities. Sec.VI concludes this work.

II. LASER PULSE AND CLUSTER PARAMETERS

We assume a laser pulse [34, 54, 55] of vector potential $\mathbf{A}_l(t') = \hat{\mathbf{x}}(E_0/\omega) \sin^2(\omega t'/2n) \cos(\omega t')$ for $0 \leq t' \leq nT$ which is polarized in \mathbf{x} and propagating in \mathbf{z} ; where $t' = t - z/c$, n = number of laser period T , $\tau = nT$ is pulse duration, and $E_0 = \sqrt{I_0}$ is field strength. Laser electric and magnetic fields $\mathbf{E}_l, \mathbf{B}_l$ read

$$\mathbf{E}_l(t') = -\frac{\partial \mathbf{A}_l}{\partial t'}, \quad \mathbf{B}_l(t') = \hat{\mathbf{z}} \times \mathbf{E}_l(t')/c \quad (1)$$

The broad-band nature of the pulse is understood from its discrete frequencies $\omega_1 = \omega, \omega_2 = (1 + 1/n)\omega, \omega_3 = (1 - 1/n)\omega$ and side-bands are significant for short pulses.

Deuterium clusters of different sizes and number of atoms $N = 2176, 7208, 17256$ are chosen. According to the Wigner-Seitz radius $r_w \approx 0.17$ nm, respective cluster radii are $R_0 = r_w N^{1/3} \approx 2.2, 3.3, 4.4$ nm. For $R_0 \ll \lambda$, the dipole approximation $z/\lambda \ll 1$ may be assumed. Single cluster is illuminated by the above laser pulse of $\lambda = 800$ nm for $n = 5$, $\tau = nT \approx 13.5$ fs ($\tau_{fwhm} \sim 5$ fs). A cluster is $\rho_i/\rho_c \approx 27.1$ times over-dense with $(\omega_M/\omega)^2 \approx 9.1$, where $\rho_c \approx 1.75 \times 10^{27} m^{-3}$ is the critical density at $\lambda = 800$ nm.

III. PARTICLE-IN-CELL (PIC) SIMULATION

We use 3D PIC simulation code [29, 30, 34, 54, 56–59] for LCI with/without ambient magnetic field \mathbf{B}_{ext} . Different deuterium clusters with $N = 2176, 7208, 17256$ are placed in a cubical computational box. Center of a cluster coincides the center of the computational box. Initially laser field $\mathbf{E}_l(t)$ ionizes all neutral atoms D to D^+ (assuming over-the-barrier ionization, OBI [60] which is valid for $I_0 > 10^{15}$ W/cm²) after reaching a critical strength $E_c = |\mathbf{E}_l(t)| = I_p^2(Z)/4Z$, where $I_p(Z)$ is the ionization potential for charge state $Z = 1$. The position and velocity of a newly born electron (after the OBI) are assumed same as the parent atom/ion conserving the momentum and energy. Subsequent movement of electrons and ions by the driving fields create/modify space-charge field $\mathbf{E}_{sc}(\mathbf{r}, t) = -\nabla\phi(\mathbf{r}, t)$ and corresponding potential $\phi(\mathbf{r}, t)$ which are time-dependent and starts from zero.

A PIC electron/ion has the same charge to mass ratio of a real electron/ion. The equation of motion of the $j|k$ -th PIC electron/ion (j for electron and k for ion) reads

$$\frac{d\mathbf{p}_{j|k}}{dt} = q_{j|k} [(\mathbf{E}_l(t) + \mathbf{E}_{sc}(\mathbf{r}_{j|k}, t)) + \mathbf{v}_{j|k} \times (\mathbf{B}_l + \mathbf{B}_{ext})] \quad (2)$$

$$\frac{d\mathbf{r}_{j|k}}{dt} = \mathbf{v}_{j|k} = \frac{\mathbf{p}_{j|k}}{\gamma_{j|k} m_{j|k}} \quad (3)$$

where $\mathbf{p}_{j|k} = m_{j|k} \mathbf{v}_{j|k} \gamma_{j|k}$, $\mathbf{v}_{j|k}$, $\mathbf{r}_{j|k}$, $m_{j|k}$, $q_{j|k}$, $\gamma_{j|k}$ are momentum, velocity, position, mass, and charge of a PIC electron/ion and $\gamma_{j|k} = \sqrt{1 + p_{j|k}^2/m_{j|k}^2 c^2}$ respectively. In the present case, $m_j = m_0 = 1, m_k = M_0 = 2 \times 1386, q_j = -1$ and $q_k = 1$ in a.u.. Poisson's equation $\nabla^2 \phi_G = -\rho_G$ is solved for ϕ_G on the numerical grid (subscript G indicates grid values of potential and charge density) with time-dependent monopole boundary condition. Interpolating ϕ_G to the particle position corresponding potential $\phi(\mathbf{r}_{j|k}, t)$ is obtained. Field $\mathbf{E}_{sc}(\mathbf{r}_{j|k}) = -\nabla\phi(\mathbf{r}_{j|k})$ is obtained by analytical differentiation [59] of interpolated $\phi(\mathbf{r}_{j|k})$ locally at $\mathbf{r}_{j|k}$. Equations (2)-(3) are solved by the velocity verlet method (VVM) using laser fields (1). VVM leads to better energy conservation and less numerical heating even for a bigger Δt , particularly for the relativistically intense driving fields. Electron-ion collisions are neglected in the current work due to high field strengths. Total absorbed energy $\mathcal{E}(t) = \sum_l q_l \phi_l + p_l^2/2m_l$ is obtained by summing over kinetic energy $KE = \sum_l p_l^2/2m_l$ and potential energy $PE = \sum_l q_l \phi_l$ of all electrons and ions. For the $n = 5$ -cycle pulse (used here) contribution of ion kinetic energy is small and total energy is

mainly due to electrons. Final absorbed energy $\mathcal{E}_A = \mathcal{E}(\tau)$ in the end the laser pulse at $\tau = nT$ is also noted. The numerical parameters in the PIC simulation (spatial and temporal resolution, grid size, number of PIC particles/cell etc.) are carefully chosen for negligible artificial numerical heating. Typically, we choose 64^3 (128^3 for bigger cluster) grid points (cells) with uniform cell size $\Delta x = \Delta y = \Delta z = 16$ a.u., time step $\Delta t = 0.1$ a.u., and approximately 15 particles/cell.

A. Hybrid-PIC

In the PIC simulation, treatment of particles crossing/leaving the boundaries of the simulation box needs a special care. Often reflecting or periodic boundary conditions are used, which preserve particles inside the simulation box and Poisson equation with appropriate boundary conditions takes care of the space-charge field $\mathbf{E}_{sc}(\mathbf{r}_{jk})$ on an inside particle. For a finite size target (e.g., cluster) in early works we have used open boundary conditions for particles, meaning that particles which leave the simulation box are free from space-charge field $\mathbf{E}_{sc}(\mathbf{r}_{jk})$. This assumption is tested valid for the short laser pulse by keeping simulation box size $L \approx 16 - 20R_0$ (typically) beyond which $\mathbf{E}_{sc} \approx 0$. It also allows particles (particularly electrons) to come back inside the box or propagate similar to direct laser acceleration (DLA) outside the box obeying (2)-(3). For a dense electron cloud outside the simulation box (in a strong ambient B_0) electron-electron interaction (repulsion) may be important for the divergence/collimation of the electron beam. Therefore, we adapt a new hybrid procedure to determine \mathbf{E}_{sc} on an electron: as long as it is inside the box, \mathbf{E}_{sc} is solely determined by the standard PIC approach; but when it is outside the box \mathbf{E}_{sc} is determined by the field due to total charge (including ions and electrons) inside the simulation box (monopole field) plus the fields due all other electrons outside the simulation box as in MD simulations[33].

IV. LASER ABSORPTION IN CLUSTER IN AMBIENT MAGNETIC FIELDS

A deuterium cluster of $N = 2176$ and $R_0 = 2.2$ nm is irradiated by $n = 5$ -cycle laser pulse of $I_0 = 7.13 \times 10^{16} \text{W/cm}^2$ in presence of ambient magnetic fields $\mathbf{B}_{ext} = B_0 \hat{\mathbf{z}}$ along the laser propagation \mathbf{z} for different values of B_0 . Figure 1 shows total absorbed energy $\overline{\mathcal{E}}_A = \mathcal{E}_A / NU_p$ per electron (TE , green) in units of U_p vs normalized electron-cyclotron frequency Ω_{c0}/ω . Note that $\Omega_{c0} = B_0$ in (a.u.). At a very low B_0 (or without B_0) absorption is very poor $\overline{\mathcal{E}}_A \approx 0.5U_p$ at the point A. It gradually increases to $\overline{\mathcal{E}}_A \approx 36U_p$ at B for ECR (vertical dashed line, where $\Omega_{c0}/\omega = 1$) and reaches a peak $\overline{\mathcal{E}}_A \approx 68U_p$ at C for $\Omega_{c0}/\omega \approx 1.25$. The ratio of absorbed energies at B and C to that at A are $\overline{\mathcal{E}}_A(B)/\overline{\mathcal{E}}_A(A) \approx 72$ and $\overline{\mathcal{E}}_A(C)/\overline{\mathcal{E}}_A(A) \approx 136$ respectively. Thus strong ambient magnetic fields may enhance laser absorption $\approx 70 - 136$ folds for a cluster. Compared to laser-atom interaction[35–37] where maximum energy of a liberated electron $\approx 3.17U_p$, these $\overline{\mathcal{E}}_A$

values in a cluster range $\approx 12 - 23$ folds. Though magnetic field does not work, it re-orientates phase-space co-ordinates $(\mathbf{r}_{jk}, \mathbf{v}_{jk})$ of a charge particle (particularly for an electron), and hence may improve rate of laser absorption obeying the relation

$$\frac{d(\gamma_{jk} m_{jk} c^2)}{dt} = q_{jk} \mathbf{v}_{jk} \cdot (\mathbf{E}_l(t) + \mathbf{E}_{sc}(\mathbf{r}_{jk}, t)) \quad (4)$$

through improved phase-matching[34] between \mathbf{v}_{jk} and the total field $\mathbf{E} = \mathbf{E}_l(t) + \mathbf{E}_{sc}(\mathbf{r}_{jk}, t)$. Equation (4) is fundamental to transfer of energy to a charge particle from the interacting fields. Self-consistent $\mathbf{E}_{sc}(\mathbf{r}_{jk}, t)$ is nonlinear in general and falls quickly as $1/r^2$ after a few cluster radius R_0 . AHR absorption[34] of laser by an electron happens within this nonlinear field and may be modified[34] by an ambient \mathbf{B}_{ext} . After coming out of the cluster via AHR (called first stage[34]) with some transverse momentum, electrons are mainly controlled by remaining $\mathbf{E}_l, \mathbf{B}_l, \mathbf{B}_{ext}$ and weak \mathbf{E}_{sc} outside, and there ECR/RECR may happen (called second stage[34]) resulting enhanced laser absorption as in Fig.1. Results of simultaneous phase-matching and frequency-matching conditions for these absorption processes are already given in Ref.[34] for similar parameters and not repeated here for the sake of conciseness.

We also partition total absorbed energy (TE , green) in electron kinetic (KE , red) and potential energy (PE , blue) in Fig.1. It shows main contribution comes from electron's kinetic energy. Acceleration of these electrons by ECR/RECR (in the second stage) resembles magnetic field assisted DLA of electrons. But, in the present case, electrons originate from the over-dense cluster, self-injected into the remaining laser field in presence of ambient \mathbf{B}_{ext} and no external injection mechanism is required. It is important to mention that most of models for DLA of electrons consider an under-dense, pre-formed plasma channel [46, 61–65] or single electron without considering particle interactions.

A. Energy distribution of electrons

Panels (A,B,C) in Fig. 2 show energy distribution of PIC electrons corresponding to chosen data points (A,B,C) in Fig.1 for $B_0 \approx 0.35\omega, \omega, 1.25\omega$ respectively. It is seen that for a given $I_0 = 7.13 \times 10^{16} \text{W/cm}^2$, energy distribution of electrons gradually modifies as B_0 increases. With a low value of B_0 (or without it, for A), more electrons (yellow region) are near lower energy $\overline{\mathcal{E}}_A \approx 0.1$, though energy tail (maximum) with a few electrons extends upto $\overline{\mathcal{E}}_A \approx 2.6$. This is the typical energy distribution of electrons one mostly finds in case of LCI with a very low B_0 (or without B_0). On the other hand, for higher B_0 values corresponding to B and C, more electrons are pushed around $\overline{\mathcal{E}}_A \approx 36U_p$ and $\overline{\mathcal{E}}_A \approx 68U_p$ respectively. Thus there is a reversal in the nature (variation) of energy distribution while passing from A to C. The integrated average energy values of $\overline{\mathcal{E}}_A$ from these distributions are found to satisfy respective values of absorption at (A,B,C) in Fig.1. These group of electrons will now be thoroughly analyzed to understand their divergence (and collimation) as a beam.

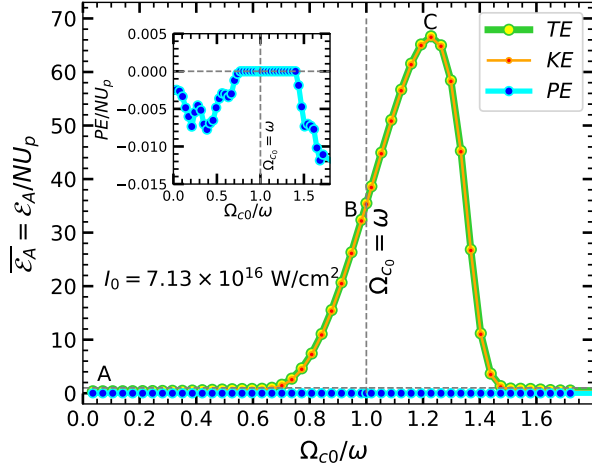


Figure 1. PIC results: Average total energy ($TE, \bar{\mathcal{E}}_A = \bar{\mathcal{E}}(\tau)$), kinetic energy (KE) and potential energy (PE) per cluster-electron vs normalized electron-cyclotron frequency Ω_{c0}/ω for a range of ambient field $|\hat{\mathbf{z}}B_{ext}| \approx (0-2\omega)$ with $n = 5$ -cycle pulse of $I_0 \approx 7.13 \times 10^{16} \text{W/cm}^2$ irradiating a deuterium cluster of $N = 2176$ and $R_0 = 2.2$ nm. Energy is shown normalized by corresponding U_p . At a low I_0 absorption peak occurs almost at the ECR condition $\Omega_{c0} = \omega$ (vertical dashed line, see Ref.[34]). Whereas, at this high $I_0 \approx 7.13 \times 10^{16} \text{W/cm}^2$, absorption is *even higher* and absorption peak is right-shifted from ECR condition $\Omega_{c0} = \omega$ due to relativistic modification of $\Omega_c = \Omega_{c0}/\gamma$ for $\gamma > 1$. Absorption peak $\approx 65U_p$ give average energy per electron $\bar{\mathcal{E}}_A \approx 0.27$ MeV. Inset shows negligibly small average PE per electron, and thus TE is mainly due to KE .

B. Angular distribution of electrons

Angular deflection of an electron (θ_r) in the position space is defined as the angle between the laser propagation in \mathbf{z} (which is also the direction of $\mathbf{B}_{ext} = B_0\hat{\mathbf{z}}$) and the transverse plane $x-y$. It is given by

$$\theta_r = \tan^{-1} \left(\frac{r_{\perp}}{z} \right); \text{ where } r_{\perp} = \sqrt{x^2 + y^2}. \quad (5)$$

Figure 3 shows histograms of electrons vs θ_r (a1,b1,c1, left column) and respective polar plots (a2,b2,c2, right column) with their normalized position r/R_0 vs θ_r corresponding to those energy spectra (A,B,C) in Fig.2. Polar co-ordinates (r, θ_r) are color-coded with their energy normalized by U_p . For lower $B_0 = 0.02$ a.u. electrons are spread over a wide angular range $\approx 0 - 175^\circ$ (Fig.3 a1). Distribution in the (r, θ_r)-plane explains that, the angular spreading contains only low energetic electrons due to weak coupling of laser to the cluster electrons at lower B_0 values (Fig.3 a2). As the magnetic field increases to $B_0 = 0.057$ a.u. (Fig.3 b1,b2) and $B_0 = 0.07$ a.u. (Fig.3 c1,c2) the electrons align themselves more towards the magnetic field direction \mathbf{z} within an angular spreading of $\Delta\theta_r < 5^\circ$. This demonstrates that the ambient magnetic field near ECR/RECR probes the ejected electrons to form a collimated beam. For $B_0 = 0.057$ a.u. and $B_0 = 0.07$ a.u., energy of most of the electrons in the collimated beam in Figs.3 (b2,c2) show maximum absorption satisfies the energy distribution peaks in Figs.2 (B,C) respectively.

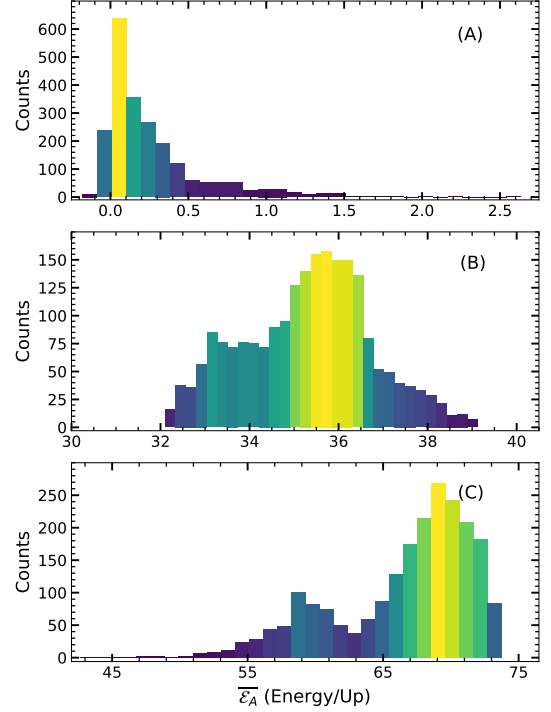


Figure 2. Energy distribution of PIC electrons (A,B,C) ejected from the deuterium cluster corresponding to the ambient magnetic fields $B_0 \approx 0.02, 0.057, 0.07$ a.u. (at A, B,C) in Fig.1. Yellow region highlights maximum electron-counts and respective energy $\bar{\mathcal{E}}_A$. Other parameters are same as in Fig.1.

The collimation of electrons can also be explained by the angular deflection (θ_p) in the momentum space with transverse momentum (p_x, p_y) and longitudinal momentum (p_z) as

$$\theta_p = \tan^{-1} \left(\frac{p_{\perp}}{p_z} \right); \text{ where } p_{\perp} = \sqrt{p_x^2 + p_y^2}. \quad (6)$$

Figure 4 shows histograms of electrons vs θ_p (a1,b1,c1, left column) and respective polar plots (a2,b2,c2, right column) with their normalized momentum p/c vs θ_p corresponding to those energy spectra in Fig.3. Co-ordinates (p, θ_p) are color-coded with their energy normalized by U_p . For $B_0 = 0.02$ a.u., there is a wide angular spread centered around $\theta_p \approx 90^\circ$, with low energetic electrons in Figs.4(a1, a2). However, for higher magnetic fields $B_0 = 0.057$ (a.u.) in Figs.4(b1, b2) and $B_0 = 0.07$ (a.u.) in Figs.4(c1, c2) collimated beams of high energetic electrons are formed in momentum space with angular spreading $\Delta\theta_p < 5^\circ$ similar to $\Delta\theta_r < 5^\circ$ in the position space. Momentum of beam electrons reach weakly relativistic values $p = \sqrt{p_{\perp}^2 + p_z^2} \approx 0.875c, 1.25c$ (b2,c2) even with short 5-cycle laser pulse of intensity $I_0 \approx 7.13 \times 10^{16} \text{W/cm}^2$.

V. EFFECTS OF CLUSTER SIZE VARIATION

In a realistic scenario, cluster size may vary. The effect of ECR/RECR with an ambient magnetic field on different cluster size is not known. Particularly, it is important to

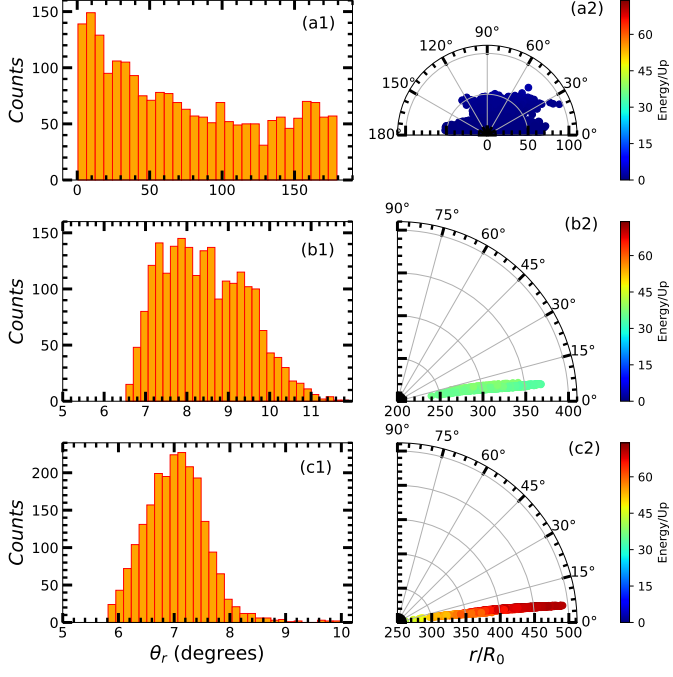


Figure 3. Histograms/distributions of angular deflection θ_r of PIC electrons (a1,b1,c1, left column) and respective polar plots (a2,b2,c2, right column) with their normalized position r/R_0 vs θ_r corresponding to those energy spectra (A,B,C) in Fig.2 for $B_0 = 0.02, 0.057, 0.07$ a.u. respectively. Polar co-ordinates (r, θ_r) are color-coded with their energy normalized by U_p . Ejected electrons propagate long distance $r = \sqrt{r_\perp^2 + z^2} \approx 375R_0, 500R_0$ (b2,c2) as collimated beams with angular spreads $\Delta\theta_r < 3^\circ$ centered around $\theta_r \approx 7 - 8.5^\circ$. Other parameters are same as in Fig.1 and Fig.2.

know whether a bigger cluster absorbs more laser energy via ECR/RECR compared to a smaller cluster of $R_0 \approx 2.2$ nm in Sec.IV. Therefore we simulate bigger deuterium clusters of $R_0 \approx 3.3, 4.4$ nm having number of atoms $N = 7208, 17256$ respectively. However, to accommodate bigger clusters as well as to obtain good accuracy, we now increase the number of computational grids to 128^3 and the simulation box size to 2048^3 a.u. in the PIC simulation keeping other simulation parameters/configurations same as the smaller cluster in Sec.IV.

Figures 5(a1,a2,a3) show the comparison of absorption per electron $\bar{\mathcal{E}}_A = \mathcal{E}_A/NU_p$, total absorption \mathcal{E}_A and outer ionized fraction N_{out}/N of electrons vs Ω_{c0}/ω of three different cluster sizes for a range of $B_0 = 0 - 2\omega$ in the end of $n = 5$ -cycle pulse of intensity $I_0 = 7.13 \times 10^{16} \text{W/cm}^2$. Here N_{out} is the number of freed electrons those have left the cluster boundary. It is evident that increasing cluster size does not significantly affect the absorption peak location (a1,a2) and value of per electron energy $\bar{\mathcal{E}}_A$ upto ECR (a1). The maximum absorption per electron [$\max(\bar{\mathcal{E}}_A)$] at the peak gradually drops to $\approx 68U_p, 59U_p, 54U_p$ as cluster size increases $R_0 = 2.2, 3.3, 4.4$ nm (a1), which is partly due to relatively less number of outer-ionized electrons (N_{out}) for the bigger cluster. The outer-ionization of $R_0 \approx 4.4$ nm cluster (a3) at this $I_0 = 7.13 \times 10^{16} \text{W/cm}^2$ is $\approx 85 - 90\%$ which means

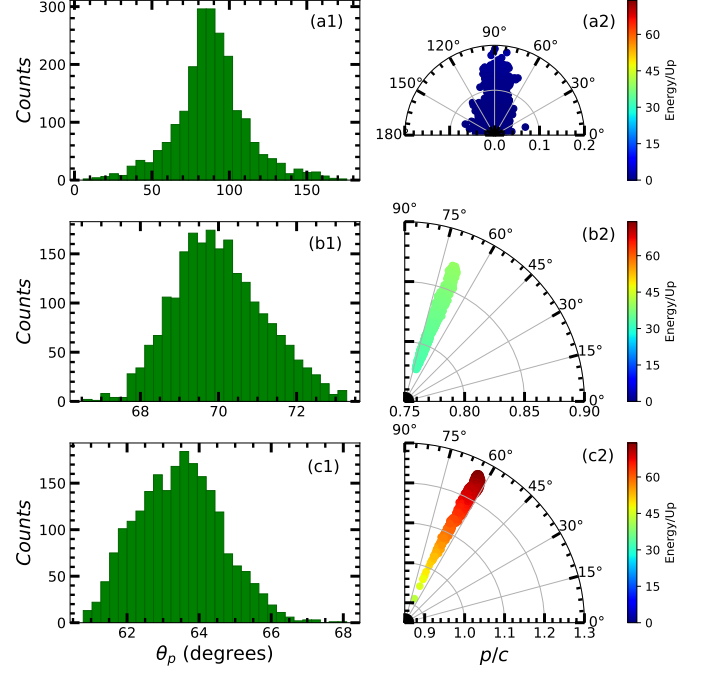


Figure 4. Histograms/distributions of angular deflection θ_p of PIC electrons (a1,b1,c1, left column) in the momentum space and respective polar plots (a2,b2,c2, right column) with their normalized momentum p/c vs θ_p corresponding to energy spectra (A,B,C) in Fig.2 for $B_0 = 0.02, 0.057, 0.07$ a.u. respectively. Polar co-ordinates (p, θ_p) are color-coded with their energy normalized by U_p . Momentum of ejected electrons reach $p = \sqrt{p_\perp^2 + p_z^2} \approx 0.875c, 1.25c$ (b2,c2) as collimated beams with angular spreads $\Delta\theta_p < 4^\circ$ centered around $\theta_p \approx 70 - 64^\circ$. Other parameters are as in Fig.1 and Fig.2.

mainly $85 - 90\%$ electrons contribute to the total energy absorption. However, for the $R_0 \approx 2.2, 3.3$ nm clusters, outer-ionization are around 100% and 98% respectively, indicating nearly all electrons contribute to the energy absorption. Additionally, restoring force on electrons due to background ions gradually increases as the cluster size increases, which yields relatively higher per electron energy (a1) at the peak $\max(\bar{\mathcal{E}}_A) \approx 68U_p$ for a smaller $R_0 \approx 2.2$ nm cluster compared to $\max(\bar{\mathcal{E}}_A) \approx 48U_p$ for a bigger $R_0 \approx 4.4$ nm cluster. *In contrast*, the total energy absorption \mathcal{E}_A by electrons (a2) gradually increases with increasing cluster size at a given B_0 and for a bigger cluster it is significantly higher at the peak due to more energy carriers (N_{out}) after the outer-ionization.

For many applications, higher flux of energetic electrons as a collimated beam may be required and bigger clusters may supply them. Therefore, in Fig.6 we plot histograms for angular distribution of electrons and corresponding polar plots (insets) for $R_0 = 3.3, 4.4$ nm clusters (as in Fig.3 with 2.2 nm cluster) corresponding to $B_0 \approx 0.057$ a.u. (at B in Fig.5a1) and $B_0 \approx 0.07$ a.u. (at C in Fig.5a1) respectively. Compared to 2.2 nm cluster (Fig.3), the angular spread $\Delta\theta_r$ is little wider for larger clusters (Fig.6), but there are now more number of energetic electrons within $\theta_r \approx 8^\circ - 12^\circ$. In

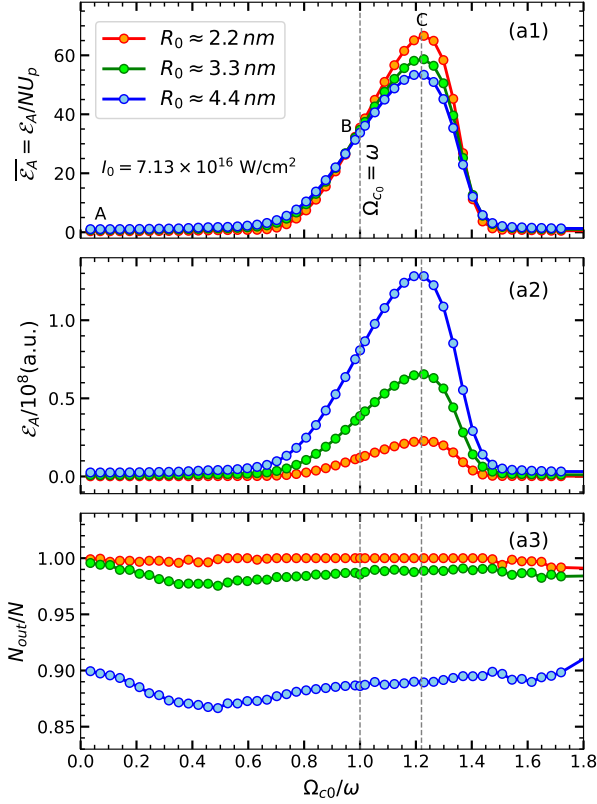


Figure 5. Results for different cluster sizes with $I_0 = 7.13 \times 10^{16} \text{ W/cm}^2$: (a1) average total energy ($\bar{\mathcal{E}}_A = \mathcal{E}_A/NU_p$) per cluster-electron in units of U_p , (a2) absorbed total energy (\mathcal{E}_A) in the cluster scaled down by 10^8 , (a3) fractional outer-ionization of electrons (N_{out}/N) vs normalized electron-cyclotron frequency Ω_{c0}/ω for a range of ambient field $|\hat{z}B_{ext}| \approx (0 - 2\omega)$ for different cluster sizes $R_0 \approx 2.2, 3.3, 4.4$ nm and respective number of atoms $N = 2176, 7208, 17256$. Other parameters are same as in Fig.1.

the case of 3.3 nm cluster for $B_0 = 0.057, 0.07$ a.u. (a1,b1, left) the range of θ_r is almost same, however the electron beam with $B_0 = 0.07$ a.u. contains higher number (≈ 3300) of energetic electrons around $\theta_r \approx 8^\circ$. Similarly for 4.4 nm cluster, due to its bigger size the energetic electron population in the collimated beam increases to $\approx 5000, 6000$ for $B_0 = 0.057, 0.07$ a.u. (a2,b2, right) around $\theta_r \approx 8^\circ$. We may conclude that the collimated electron beams become more intense with greater number of energetic electrons as cluster size increases which may not be possible without ambient B_0 .

A. Effects at high intensity

Results in previous sections are obtained with $I_0 = 7.13 \times 10^{16} \text{ W/cm}^2$. In case of 4.4 nm cluster (Fig.5a3) nearly 10-15% electrons are still within the cluster at this intensity. We now perform PIC simulations at a higher $I_0 = 1.83 \times 10^{17} \text{ W/cm}^2$ (still in the non-relativistic regime) for all three cluster sizes $R_0 = 2.2, 3.3, 4.4$ nm, keeping other parameters same as in Fig.5. Results of absorption per electron $\bar{\mathcal{E}}_A =$

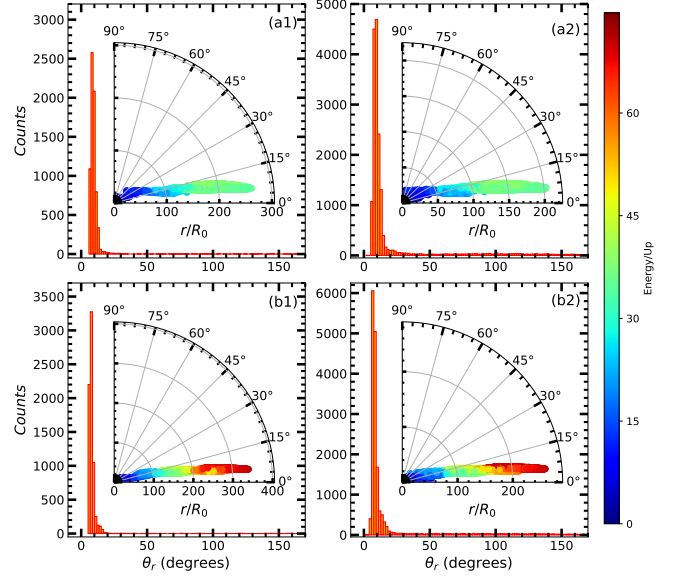


Figure 6. Results for different cluster sizes with $I_0 = 7.13 \times 10^{16} \text{ W/cm}^2$: Histograms/distributions of angular deflection θ_r of PIC electrons and respective polar plots (insets) with their r/R_0 vs θ_r corresponding to data points at (B,C) in Fig.5a1 with $B_0 = 0.057, 0.07$ a.u. for $R_0 \approx 3.3$ nm cluster with $N = 7208$ atoms (a1,b1, left column) and $R_0 \approx 4.4$ nm cluster with $N = 17256$ atoms (a2,b2, right column) respectively. Polar co-ordinates (r, θ_r) of electrons (insets) are color-coded with their energy normalized by U_p . Ejected electrons propagate long distance $r = \sqrt{r_\perp^2 + z^2} \approx 350R_0, 280R_0$ (b1,b2) as collimated beams with angular spreads $\Delta\theta_r < 3^\circ$ centered around $\theta_r \approx 7 - 8^\circ$. Other parameters are same as in Fig.1.

$\bar{\mathcal{E}}_A/NU_p$ in U_p , total absorption \mathcal{E}_A and outer ionized fraction N_{out}/N of electrons vs Ω_{c0}/ω are shown in Fig.7. Compared to Fig.5, per electron energy $\bar{\mathcal{E}}_A$ for ejected electrons from different clusters are nearly same (Fig.7a1) and maximum absorption per electron now ranges $\bar{\mathcal{E}}_A \approx 44 - 42U_p$ as cluster size increases $R_0 = 2.2 - 4.4$ nm, but outer-ionization reaches 100% for all clusters (Fig.7a3) at this higher intensity. Total absorption \mathcal{E}_A in each cluster (Fig.7a2) increases more than two times than in Fig.5a2. If we compare the ratio of maximum absorption (Fig.7a2) for different clusters, we find $\max(\mathcal{E}_A) \approx 0.4 : 1.3 : 2.8 \approx 1 : 3.325 : 6.9$ which scales with the number electrons in the cluster as $N \approx 2176 : 7208 : 17256 \approx 1 : 3.3 : 7.9$. Thus N vs $\max(\mathcal{E}_A)$ is almost linear at a very high I_0 when outer-ionization is 100%.

In Fig.8 we compare the distribution of ejected electrons in (r, θ_r) plane (as in Figs.3,6) for three different cluster sizes (column wise) corresponding to points (B,C) in Fig.7 with $B_0 = 0.057, 0.078$ a.u. (top, bottom). We find respective electron beams are even more collimated within an angular range of $\Delta\theta_r \approx 3^\circ - 4^\circ$. Also, with increasing cluster size, electron beams are more intense with greater number of energetic electrons. At a very high I_0 and ambient B_0 near ECR/RECR, electron distribution for a bigger cluster becomes very similar to that of a small cluster in the regime of 100% outer-ionization.

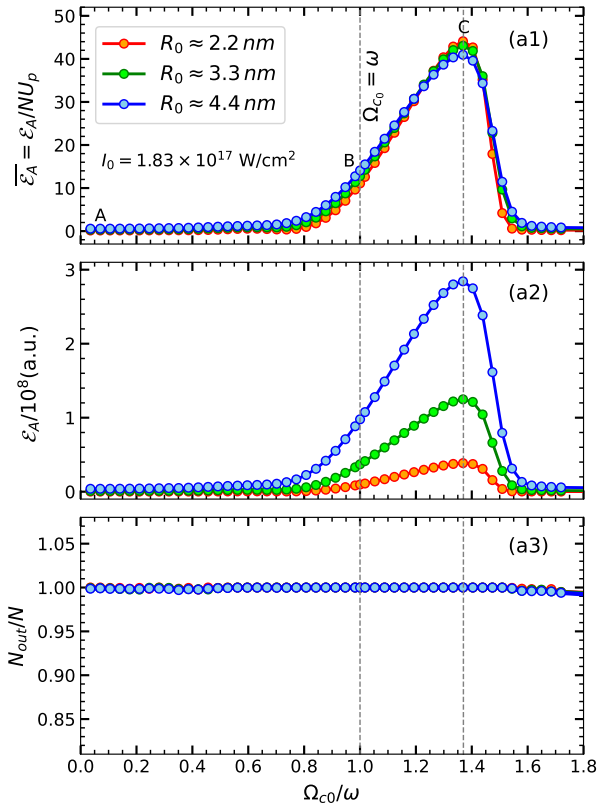


Figure 7. Results for different cluster size with $I_0 = 1.83 \times 10^{17}$ W/cm²: (a1) average total energy ($\bar{\mathcal{E}}_A = \mathcal{E}_A / NU_p$) per cluster-electron in units of U_p , (a2) absorbed total energy (\mathcal{E}_A) in the cluster scaled down by 10^8 , (a3) fractional outer-ionization of electrons (N_{out}/N) vs normalized electron-cyclotron frequency Ω_{c0}/ω for a range of ambient field $|\hat{z}B_{ext}| \approx (0 - 2\omega)$ for different cluster sizes $R_0 \approx 2.2, 3.3, 4.4$ nm and respective number of atoms $N = 2176, 7208, 17256$. Note that $I_0 = 1.83 \times 10^{17}$ W/cm² corresponds to greater $U_p = 402.26$ a.u. compared to Fig.5. Other parameters are same as in Fig.1.

VI. CONCLUSION

We study interaction of intense 800 nm, 5-fs (fwhm) broadband laser pulses of different intensities $I_0 = 7.13 \times 10^{16} - 1.83 \times 10^{17}$ W/cm² with deuterium clusters of various sizes

(radius $R_0 \approx 2.2 - 4.4$ nm) in presence of ambient magnetic fields of strengths $B_0 = 0 - 2\omega$ along the laser propagation direction \mathbf{z} using 3D hybrid-PIC simulations. Here laser absorption occurs in two stages via AHR (1st stage) and electron cyclotron resonance (ECR) or relativistic ECR (RECR) processes (2nd stage). Auxiliary B_0 enhances coupling of laser to cluster-electrons via improved frequency-matching for ECR/RECR as well as phase-matching[34] for prolonged duration of the pulse (which are also checked for bigger clusters, but not repeated here for conciseness) and the average absorbed energy per electron $\bar{\mathcal{E}}_A$ jumps to $\bar{\mathcal{E}}_A \approx 36 - 70 U_p$ which is significant. Otherwise $\bar{\mathcal{E}}_A$ is mostly limited around $\bar{\mathcal{E}}_A \approx 0.5 - 3 U_p$ without B_0 . Increasing the cluster size ($R_0 \approx 2.2 \rightarrow 4.4$ nm) per electron energy $\bar{\mathcal{E}}_A$ remains almost same ($\bar{\mathcal{E}}_A \approx 36 - 70 U_p$) near ECR/RECR, but net absorption increases almost linearly with number of electrons (N) in the regime of 100% outer-ionization at high intensities.

We further analyze the energy distribution of ejected electrons as well as their angular distribution in the position space and in the momentum space. We find that laser coupled electrons form a nearly mono-energetic, weakly relativistic collimated beam that traverse a few hundreds of R_0 (or on the order of λ) in presence of an ambient magnetic field near ECR/RECR which may not be possible only with the laser field. Also, as the cluster size increases, intensity of electron beam increases with greater number of energetic electrons at a restricted angle of $\theta_f \approx 7^\circ - 10^\circ$ w.r.t. \mathbf{z} direction for $I_0 = 7.13 \times 10^{16} - 1.83 \times 10^{17}$ W/cm².

This work may find importance for the fast ignition technique of inertial confinement fusion where intense collimated relativistic electron beam (REB) is required to be transported deep inside the matter with less divergence, laser-driven electron accelerators, ultra-short x-ray sources for radiation therapy and other medical applications.

ACKNOWLEDGEMENTS

Numerical simulation works have been performed in Antya Linux cluster of HPC facility at IPR. Authors acknowledge Dr. Devendra Sharma for careful reading of the manuscript.

-
- [1] T. Ditmire, J. W. G. Tisch, E. Springate, M. B. Mason, N. Hay, J. P. Marangos, and M. H. R. Hutchinson, Phys. Rev. Lett. **78**, 2732 (1997).
 - [2] T. Ditmire, E. Springate, J. W. G. Tisch, Y. L. Shao, M. B. Mason, N. Hay, J. P. Marangos, and M. H. R. Hutchinson, Phys. Rev. A **57**, 369 (1998).
 - [3] T. Ditmire, J. W. G. Tish, E. Springate, M. B. Mason, N. Hay, J. Marangos, and M. H. R. Hutchinson, Nature (London) **386**, 54 (1997).
 - [4] M. Lezius, S. Dobosz, D. Normand, and M. Schmidt, Phys. Rev. Lett. **80**, 261 (1998).
 - [5] R. Rajeev, T. M. Trivikram, K. P. M. Rishad, V. Narayanan, E. Krishnakumar, and M. Krishnamurthy, Nat Phys. **9**, 185 (2013).
 - [6] L. M. Chen, J. J. Park, K. H. Hong, I. W. Choi, J. L. Kim, J. Zhang, and C. H. Nam, Physics of Plasmas **9**, 3595 (2002).
 - [7] Y. L. Shao, T. Ditmire, J. W. G. Tisch, E. Springate, J. P. Marangos, and M. H. R. Hutchinson, Phys. Rev. Lett. **77**, 3343 (1996).
 - [8] E. Springate, S. A. Aseyev, S. Zamith, and M. J. J. Vrakking, Phys. Rev. A **68**, 053201 (2003).
 - [9] L. M. Chen, J. J. Park, K.-H. Hong, J. L. Kim, J. Zhang, and C. H. Nam, Phys. Rev. E **66**, 025402 (2002).

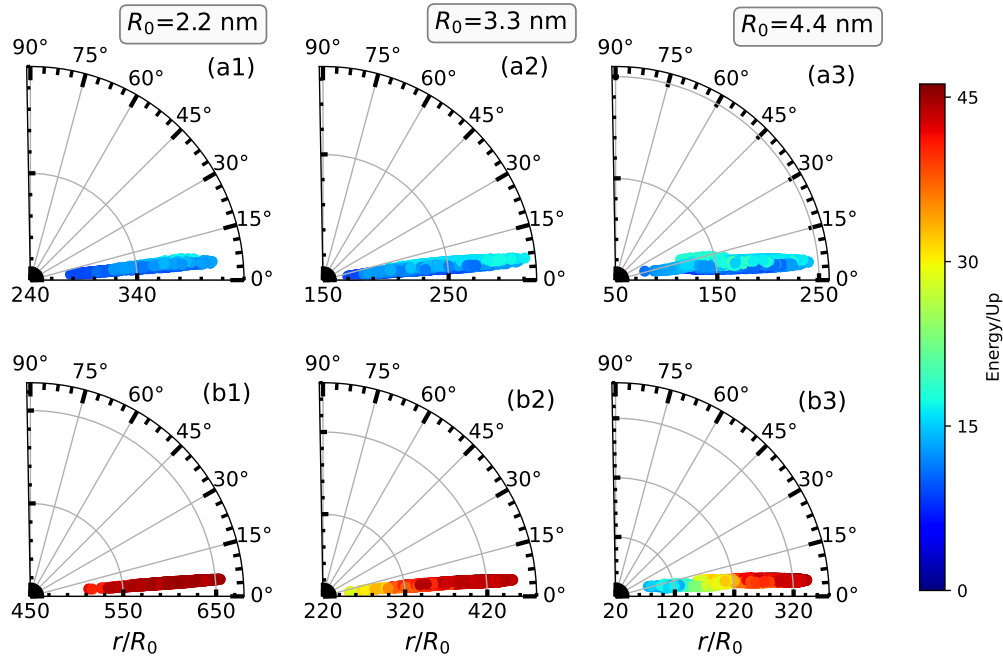


Figure 8. Results for different cluster size (column wise) with higher $I_0 = 1.83 \times 10^{17} \text{ W/cm}^2$: Angular distribution of PIC electrons in the polar-plane with r/R_0 vs θ_r corresponding to those data points at (B,C) in Fig.7 for $B_0 = 0.057, 0.078$ a.u. (top,bottom) respectively. Panels (a1,b1, left column) for 2.2 nm cluster (2176 atoms), (a2,b2, middle column) for 3.3 nm cluster (7208 atoms) and (a3,b3, right column) for 4.4 nm cluster (17256 atoms). Polar co-ordinates (r, θ_r) of electrons are color-coded with their energy normalized by U_p . Ejected electrons propagate long distance beyond $r = \sqrt{r_{\perp}^2 + z^2} \approx 650R_0, 430R_0, 330R_0$ (b1,b2,b3) as collimated beams with angular spreads $\Delta\theta_r < 3^\circ$ centered around $\theta_r \approx 6 - 7^\circ$. Other parameters are same as in Fig.1 and Fig.2.

- [10] A. McPherson, B. D. Thompson, A. B. Borisov, K. Boyer, and C. K. Rhodes, *Nature* **370**, 631 (1994).
- [11] L. M. Chen, F. Liu, W. M. Wang, M. Kando, J. Y. Mao, L. Zhang, J. L. Ma, Y. T. Li, S. V. Bulanov, T. Tajima, Y. Kato, Z. M. Sheng, Z. Y. Wei, and J. Zhang, *Phys. Rev. Lett.* **104**, 215004 (2010).
- [12] J. Jha, D. Mathur, and M. Krishnamurthy, *Journal of Physics B: Atomic, Molecular and Optical Physics* **38**, L291 (2005).
- [13] F. Dorchies, T. Caillaud, F. Blasco, C. Bonté, H. Jouin, S. Micheau, B. Pons, and J. Stevefelt, *Phys. Rev. E* **71**, 066410 (2005).
- [14] V. Kumarappan, M. Krishnamurthy, D. Mathur, and L. C. Tribedi, *Phys. Rev. A* **63**, 023203 (2001).
- [15] C. Rose-Petruck, K. J. Schafer, K. R. Wilson, and C. P. J. Barty, *Phys. Rev. A* **55**, 1182 (1997).
- [16] D. Bauer and A. Macchi, *Phys. Rev. A* **68**, 033201 (2003).
- [17] C. Siedschlag and J. M. Rost, *Phys. Rev. A* **67**, 013404 (2003).
- [18] E. M. Snyder, S. A. Buzza, and A. W. Castleman, Jr., *Phys. Rev. Lett.* **77**, 3347 (1996).
- [19] K. Ishikawa and T. Blenski, *Phys. Rev. A* **62**, 063204 (2000).
- [20] F. Megi, M. Belkacem, M. A. Bouchene, E. Suraud, and G. Zwicknagel, *Journal of Physics B: Atomic, Molecular and Optical Physics* **36**, 273 (2003).
- [21] C. Jungreuthmayer, L. Ramunno, J. Zanghellini, and T. Brabec, *IOP Publishing* **38**, 3029 (2005).
- [22] D. Bauer, *Journal of Physics B: Atomic, Molecular and Optical Physics* **37**, 3085 (2004).
- [23] T. Ditmire, T. Donnelly, A. M. Rubenchik, R. W. Falcone, and M. D. Perry, *Phys. Rev. A* **53**, 3379 (1996).
- [24] I. Last and J. Jortner, *Phys. Rev. A* **60**, 2215 (1999).
- [25] U. Saalmann and J.-M. Rost, *Phys. Rev. Lett.* **91**, 223401 (2003).
- [26] T. Fennel, G. F. Bertsch, and K.-H. Meiwes-Broer, *The European Physical Journal D - Atomic, Molecular, Optical and Plasma Physics* **29**, 367 (2004).
- [27] P. Mulser and M. Kanopathipillai, *Phys. Rev. A* **71**, 063201 (2005).
- [28] P. Mulser, M. Kanopathipillai, and D. H. H. Hoffmann, *Phys. Rev. Lett.* **95**, 103401 (2005).
- [29] M. Kundu and D. Bauer, *Phys. Rev. A* **74**, 063202 (2006).
- [30] M. Kundu and D. Bauer, *Phys. Rev. Lett.* **96**, 123401 (2006).
- [31] I. Kostyukov and J.-M. Rax, *Phys. Rev. E* **67**, 066405 (2003).
- [32] T. Taguchi, T. M. Antonsen, and H. M. Milchberg, *Phys. Rev. Lett.* **92**, 205003 (2004).
- [33] S. S. Mahalik and M. Kundu, *Physics of Plasmas* **23**, 123302 (2016).
- [34] K. Swain, S. S. Mahalik, and M. Kundu, *Scientific Reports* **12**, 11256 (2022).
- [35] P. Moreno, L. Plaja, and L. Roso, *Europhysics Letters (EPL)* **28**, 629 (1994).
- [36] P. Moreno, L. Plaja, and L. Roso, *Phys. Rev. A* **55**, R1593 (1997).
- [37] M. Lein and J. M. Rost, *Phys. Rev. Lett.* **91**, 243901 (2003).
- [38] M. Shaikh, A. D. Lad, K. Jana, D. Sarkar, I. Dey, and G. R. Kumar, *Plasma Physics and Controlled Fusion* **59**, 014007 (2016).
- [39] V. V. Ivanov, A. V. Maximov, R. Betti, L. S. Leal, J. D. Moody, K. J. Swanson, and N. A. Huerta, *Matter and Radiation at Extremes* **6**, 046901 (2021), <https://doi.org/10.1063/5.0042863>.
- [40] S. Fujioka, Z. Zhang, K. Ishihara, K. Shigemori, Y. Hirouaka, T. Johzaki, A. Sunahara, N. Yamamoto, H. Nakashima, T. Watanabe, H. Shiraga, H. Nishimura, and H. Azechi, *Sci-*

- tific Reports **3**, 1170 (2013).
- [41] D. Nakamura, A. Ikeda, H. Sawabe, Y. H. Matsuda, and S. Takeyama, Review of Scientific Instruments **89**, 095106 (2018), <https://doi.org/10.1063/1.5044557>.
- [42] M. Murakami, J. J. Honrubia, K. Weichman, A. V. Arefiev, and S. V. Bulanov, Scientific Reports **10**, 16653 (2020).
- [43] T. C. Wilson, Z.-M. Sheng, B. Eliasson, and P. McKenna, Plasma Physics and Controlled Fusion **63**, 084001 (2021).
- [44] A. Longman and R. Fedosejevs, Phys. Rev. Research **3**, 043180 (2021).
- [45] Y. Shi, H. Qin, and N. J. Fisch, Physics of Plasmas **25**, 055706 (2018), <https://doi.org/10.1063/1.5017980>.
- [46] Z. Gong, F. Mackenroth, T. Wang, X. Q. Yan, T. Toncian, and A. V. Arefiev, Phys. Rev. E **102**, 013206 (2020).
- [47] K. Weichman, A. P. L. Robinson, M. Murakami, and A. V. Arefiev, New Journal of Physics **22**, 113009 (2020).
- [48] M. Tatarakis, I. Watts, F. N. Beg, E. L. Clark, A. E. Dangor, A. Gopal, M. G. Haines, P. A. Norreys, U. Wagner, M.-S. Wei, M. Zepf, and K. Krushelnick, Nature **415**, 280 (2002).
- [49] M. Tatarakis, A. Gopal, I. Watts, F. N. Beg, A. E. Dangor, K. Krushelnick, U. Wagner, P. A. Norreys, E. L. Clark, M. Zepf, and R. G. Evans, Physics of Plasmas **9**, 2244 (2002).
- [50] S. L. Shapiro and S. A. Teukolsky, *Black holes, white dwarfs, and neutron stars : the physics of compact objects* (1983).
- [51] T. Iwawaki, H. Habara, S. Baton, K. Morita, J. Fuchs, S. Chen, M. Nakatsutsumi, C. Rousseaux, F. Filippi, W. Nazarov, and K. A. Tanaka, Physics of Plasmas **21**, 113103 (2014), <https://doi.org/10.1063/1.4900868>.
- [52] S. Malko, X. Vaisseau, F. Perez, D. Batani, A. Curcio, M. Ehret, J. Honrubia, K. Jakubowska, A. Morace, J. J. Santos, and L. Volpe, Scientific Reports **9**, 14061 (2019).
- [53] Y. Malkov, A. Stepanov, D. Yashunin, L. Pugachev, P. Levashov, N. Andreev, K. Platonov, and A. Andreev, High power Laser Science and Engineering **1**, 80 (2013).
- [54] M. Kundu, P. K. Kaw, and D. Bauer, Phys. Rev. A **85**, 023202 (2012).
- [55] S. S. Mahalik and M. Kundu, Phys. Rev. A **97**, 063406 (2018).
- [56] M. Kundu, S. V. Popruzhenko, and D. Bauer, Phys. Rev. A **76**, 033201 (2007).
- [57] S. V. Popruzhenko, M. Kundu, D. F. Zaretsky, and D. Bauer, Phys. Rev. A **77**, 063201 (2008).
- [58] M. Kundu and D. Bauer, Physics of Plasmas **15**, 033303 (2008).
- [59] M. Kundu, *Energy absorption, ionization, and harmonic emission in laser-irradiated atomic clusters*, Ph.D. thesis, Ruprecht-Karls-Universität, Heidelberg (2007).
- [60] H. Bethe and E. Salpeter, *Quantum Mechanics of One and Two Electron Atoms* (Springer, Berlin, 1957).
- [61] A. V. Arefiev, A. P. L. Robinson, and V. N. Khudik, Journal of Plasma Physics **81**, 475810404 (2015).
- [62] A. Pukhov, Z.-M. Sheng, and J. Meyer-ter Vehn, Physics of Plasmas **6**, 2847 (1999), <https://doi.org/10.1063/1.873242>.
- [63] G. D. Tsakiris, C. Gahn, and V. K. Tripathi, Physics of Plasmas **7**, 3017 (2000), <https://doi.org/10.1063/1.874154>.
- [64] H. S. Ghotra and N. Kant, Physics of Plasmas **23**, 013101 (2016).
- [65] H. S. Ghotra and N. Kant, Laser Physics Letters **15**, 066001 (2018).